

Contents lists available at ScienceDirect

Soil Dynamics and Earthquake Engineering

journal homepage: www.elsevier.com/locate/soildyn





Effect of soil gradation on embankment response during liquefaction: A centrifuge testing program

Trevor J. Carey ^{a,*}, Anna Chiaradonna ^b, Nathan C. Love ^c, Daniel W. Wilson ^d, Katerina Ziotopoulou ^c, Alejandro Martinez ^c, Jason T. DeJong ^c

- ^a Department of Civil Engineering, The University of British Columbia, Vancouver, BC, Canada
- b Department of Civil, Construction, Architectural, and Environmental Engineering, University of L'Aquila, L'Aquila, Italy
- E Department of Civil and Environmental Engineering, University of California at Davis, Davis, CA, USA
- ^d Center for Geotechnical Modeling, University of California at Davis, Davis, CA, USA

ARTICLE INFO

Keywords: Well graded soil Liquefaction Centrifuge testing Soil gradation Cone penetration Slope stability Embankment Earthquake Dynamic performance

ABSTRACT

This paper describes a centrifuge study undertaken to investigate how sand gradation affects the system-level performance of embankments subjected to strong shaking. Current analysis and design practices are primarily based on knowledge from case history records of liquefaction, with the majority of those from sites consisting of clean, poorly graded sands. The narrow range of gradation characteristics represented in the case history database poses a challenge during the analysis of embankment structures traditionally constructed with, or founded on, more broadly graded soils. The tests herein were designed to elucidate how embankments uniformly constructed with a well graded and poorly graded sand perform differently during earthquake shaking. A centrifuge experiment test program was developed and conducted using the 9-m-radius centrifuge at the UC Davis Center for Geotechnical Modeling. The experiment design consisted of two submerged 10-degree embankments positioned side-by-side in the same rigid model container, with one embankment constructed with poorly graded sand and the other with well graded sand. The embankments were dry pluviated to the same relative density, but the absolute densities of the sands were different. The embankments were identically instrumented with dense arrays of in-situ sensors beneath the level ground above the slope and in the mid-slope to measure the dynamic response during liquefaction. Results showed that embankments constructed at equal relative densities would both liquefy (i.e., r_u reach 1.0), but deformations were less severe for the embankments constructed with the well graded sand. Greater resistance to the generation and faster dissipation of excess porewater pressures, coupled with stronger dilatancy of the well graded sand increased embankment stability, curtailing liquefaction-induced deformations.

1. Introduction

Liquefaction of clean, poorly graded sands has been cited as the cause of several notable failures during earthquake shaking [1–3]. As a result, much of the research, and basis for the understanding of liquefaction triggering and consequences have been established using poorly graded sands as a representative test soil. These prior research efforts span laboratory element testing [4–6], system-level geotechnical centrifuge experiments [7–9], and field testing [10]. However, poorly graded sands only represent a portion of the potentially liquefiable sands found in the built environment. Observations of liquefaction in gravelly

or well graded soils have been documented [11–14], but the case history database is limited. The lack of a diverse catalog of sand gradations presents a challenge during the seismic assessment of embankment systems since the dynamic behavior of well graded soils is poorly understood.

A prior study by Pires-Sturm and DeJong [15] examined the dynamic behavior of different gradation sands in a series of level ground 1-m radius centrifuge experiments. The gradations were manufactured from four poorly graded sands with median grain size diameters ranging from 0.13 to 2.58 mm using soils sourced from the same geologic formation. The coefficient of uniformity (C_u) for the manufactured

E-mail addresses: trevor.carey@civil.ubc.ca (T.J. Carey), anna.chiaradonna1@univaq.it (A. Chiaradonna), nclove@ucdavis.edu (N.C. Love), dxwilson@ucdavis.edu (D.W. Wilson), kziotopoulou@ucdavis.edu (K. Ziotopoulou), amart@ucdavis.edu (A. Martinez), jdejong@ucdavis.edu (J.T. DeJong).

^{*} Corresponding author.

100A 25ABCD

Fig. 1. Photos of the test soils shown with a 6 mm CPT for scale. a.) the poorly graded 100A sand and b.) the well graded 25ABCD sand.

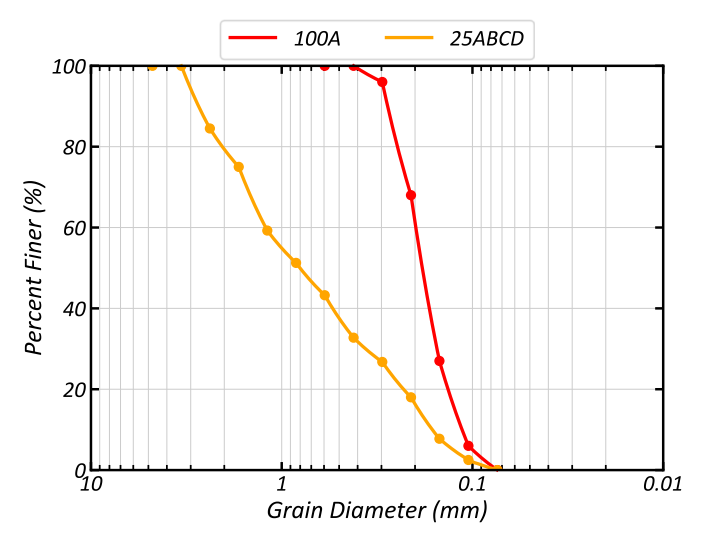


Fig. 2. Grain size distributions of the two sand mixtures.

 $\begin{tabular}{ll} \textbf{Table 1}\\ \textbf{Minimum, maximum, and test void ratios for the 100A and 25ABCD sand.} \end{tabular}$

Sand	C_{u}	D ₁₀ (mm)	D ₅₀ (mm)	e_{min}	e_{max}	$\begin{array}{l} e @ \\ D_r = \\ 40\% \end{array}$	e @ D _r = 63%	G_s
100A	1.68	0.12	0.18	0.579	0.881	0.76	0.69	2.62
25ABCD	7.44	0.16	0.8	0.303	0.544	0.45	0.39	2.61

gradations ranged from 1.68 to 7.86. Pires-Sturm and DeJong [15] observed as the sand gradation became increasingly well graded, they exhibit more pronounced dilative tendencies and reduced volumetric strains during post-liquefaction reconsolidation.

A centrifuge test program was developed to understand how gradation affects system-level performance during liquefaction. The focus of the testing program was comparing the dynamic response of embankment systems constructed with poorly graded and well graded sands. This paper describes two centrifuge experiments performed at the UC Davis Center for Geotechnical Modeling (CGM) on the 9-m-radius centrifuge. Novel centrifuge experimental hardware and measurement techniques were developed as part of this work to characterize the dynamic performance and deformation response mechanisms.

Two embankments were positioned side-by-side in the same rigid model container in each centrifuge experiment. One embankment was constructed with a poorly graded sand and the other with a well graded sand. Both embankments were dry pluviated to the same relative density. The two centrifuge experiments differed in embankment relative

densities (D_r) , with test #1 performed at $D_r=63\%$ and test #2, $D_r=40\%$. Earthquake shaking was simulated using a suite of 1 Hz motions with increasing intensity during successive events. Dense arrays of accelerometers and porewater pressure transducers were used to record insitu behaviors. Located exterior of the model container along the length of each embankment were highspeed cameras, recording liquefaction-induced deformations through the transparent sidewalls of the model container. Displacement time histories were calculated using the digital image correlation software GEOPIV-RG.

2. Soils and test design

Images of the two sand mixtures used for this study are shown in Fig. 1 with a 6 mm diameter CPT for scale. The poorly graded sand in this study had a C_0 of 1.68, and the well graded sand had a C_0 of 7.45. Following established naming convention from the literature, the poorly graded sand will be referred to as 100A and the well graded sand as 25ABCD henceforth [16]. The grain size distributions are provided in Fig. 2, while Table 1 lists the void ratios and dry densities for the $D_r =$ 63% and $D_r = 40\%$ tests. Additional physical and mechanical properties of the two sand gradations are summarized by Sturm [16]. The sands used to create the two mixtures were sourced from the Cape May Formation near Mauricetown, New Jersey, and these sands were selected since the particle size, shape, and mineralogy were consistent with naturally deposited sands found in the built environment [16]. The 25ABCD sand contains 25% by mass of four different poorly graded sands. The two test sand gradations have similar D₁₀ grain sizes, but the void ratios were lower for the 25ABCD sand, reducing the hydraulic conductivity [17]. The hydraulic conductivity (k) was measured in the laboratory using a falling head permeability test for the specimen density of $D_r = 63\%$. The measured permeabilities were k = 0.011 cm/s for the 25ABCD sand and $k=0.021\ cm/s$ for the 100A sand.

The experiments were designed for and tested on the 9-m-radius centrifuge at the UC Davis CGM for a centrifugal acceleration of 40 g and followed conventional centrifuge scaling laws [18]. Model saturation was done under vacuum using Hydroxypropyl methylcellulose fluid with a viscosity (µ *) of 40 cSt to minimize scaling conflicts with diffusion time of excess porewater pressures. Fig. 3 illustrates the test design configuration in plan and elevation views for model scale units. Each experiment consisted of two 10°-sloped and submerged embankments positioned side-by-side in the same rigid model container. One embankment consisted of a uniform profile of 100A sand and the other a uniform profile of 25ABCD sand. The prototype lengths of the level ground segments were 19.8 m, and the slope was 30.9 m. The depths of the upslope and downslope level ground segments were 14 and 8 m, respectively. Both embankments had identical geometries and instrumentation and were separated by a 19 mm thick aluminum wall. By positioning the embankments parallel to each other, the input motion was applied with the same polarity to each embankment. This allowed for a more robust time base comparison of dynamic responses.

Underlain each embankment was a dense layer ($D_r > 90\%$) of 100A sand compacted into place. Each embankment was prepared using dry pluviation in a series of 2.5 cm thick lifts. The 10-degree slope of the embankment geometry was achieved by vacuuming excess soil using a wooden template. A 0.5 cm cap of coarse sand ($D_{50} = 1.31$ mm) was added to provide confinement for the surface accelerometers (i.e., AH6 and AH11 in Fig. 3) while not impeding upward seepage following liquefaction. The cap layer was verified to abide by Terzaghi's piping and permeability criteria for the 100A and 25ABCD sand mixtures.

In this work, the $D_r=63\%$ and $D_r=40\%$ centrifuge experiments are referenced as test #1 and test #2, respectively. The embankments constructed with the different soil types are referenced as, A for 100A, and B for 25ABCD. Therefore, test #1A, test #1B, test #2A and test #2B references the $D_r=63\%\text{-}100\text{A},\,D_r=63\%\text{-}25\text{ABCD},\,D_r=40\%\text{-}100\text{A}$ and $D_r=40\%\text{-}25\text{ABCD}$ embankments, respectively.

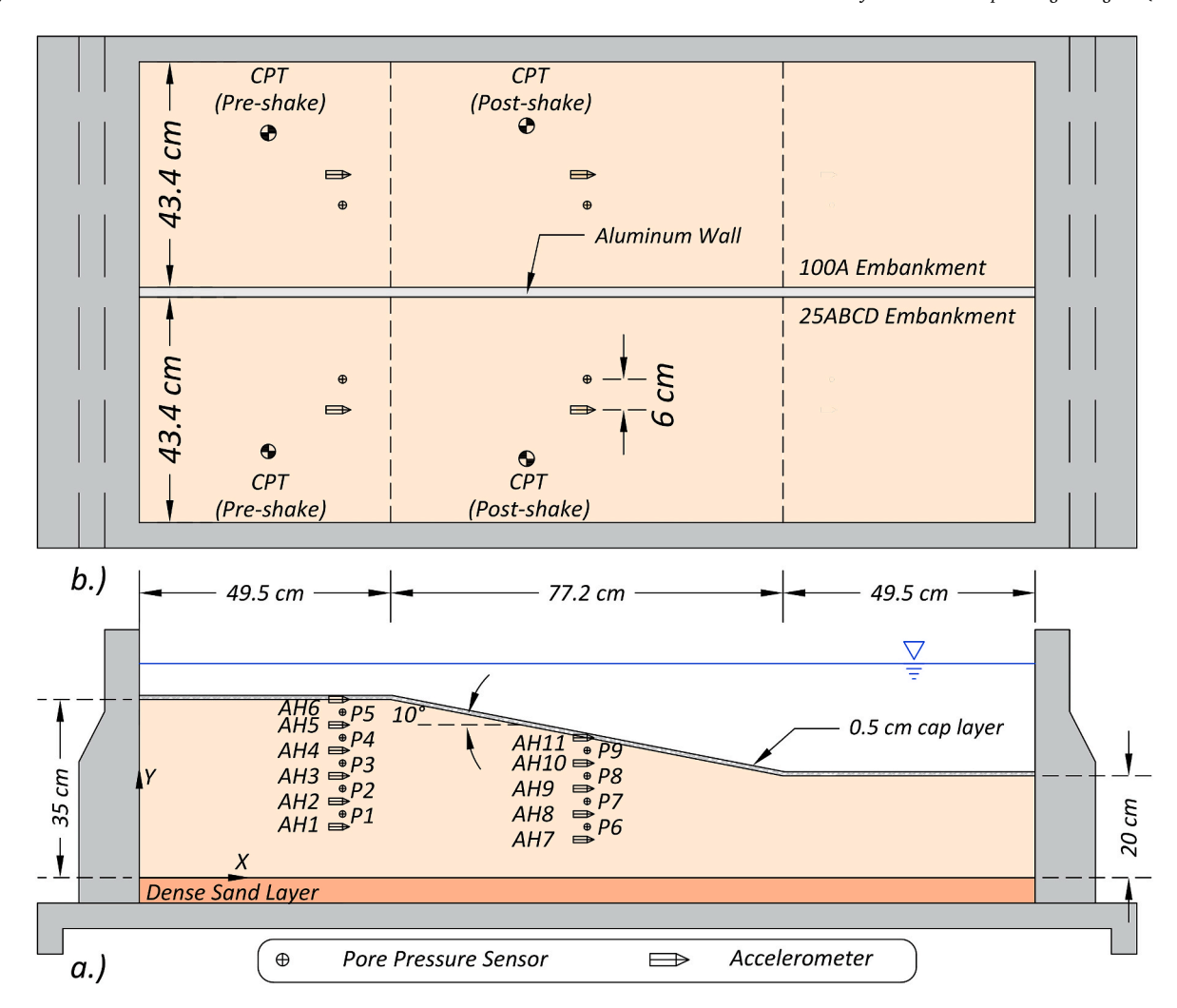


Fig. 3. Schematic of the centrifuge model used for both experiments. a) elevation view and b) plan view. All dimensions are listed in model scale.

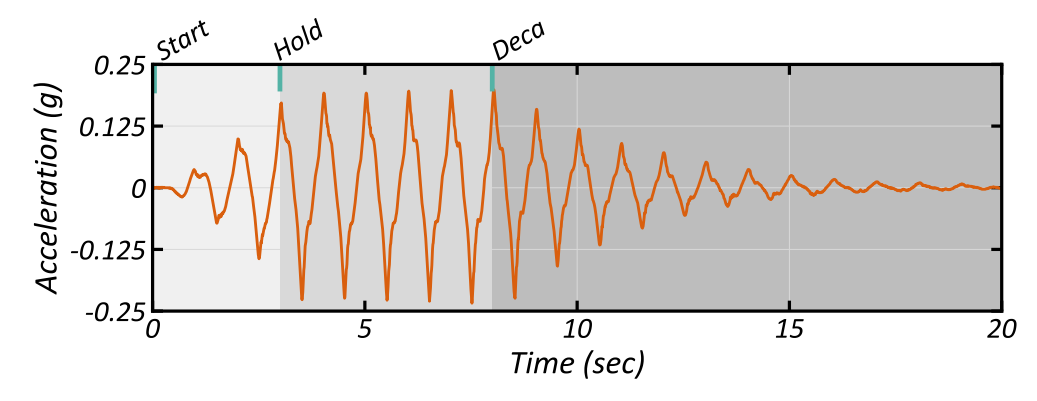


Fig. 4. Achieved model container motion for shake 3 with the beginning of three phases of the motion labeled.

 $\begin{tabular}{ll} \textbf{Table 2} \\ \textbf{Number of cycles for each shake delineated by the three phases of the input motion.} \\ \end{tabular}$

Shake	Number of Cycles						
	Build	Hold	Decay	Total			
1	3	3	1	7			
2	3	4	1	8			
3	3	5	12	20			
4	3	5	12	20			

2.1. Ground motion sequence

The ground motion sequence for both tests consisted of four successive shaking events with increasing energy. The synthetic one-dimensional horizontal input motions consisted of multiple cycles of 1 Hz prototype loading. The 1 Hz frequency was selected since it was lower than the fundamental frequencies of the two embankments (discussed later), minimizing resonance.

The cyclic amplitude of the 1 Hz waveform consisted of three sequential continuous phases. The phases were: (1) linearly increasing

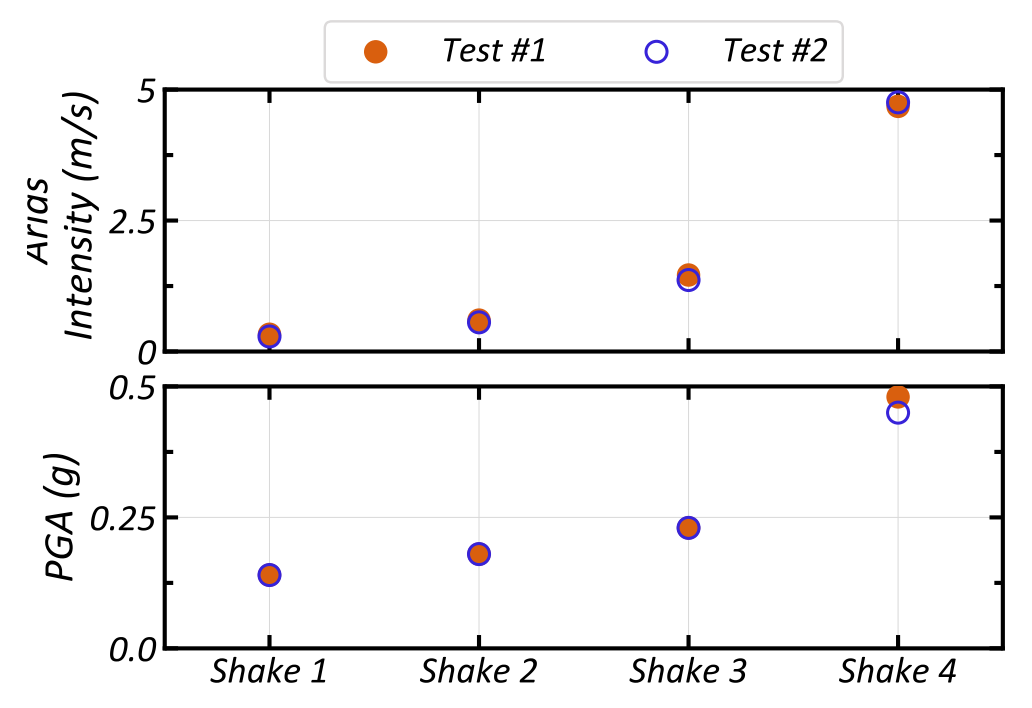


Fig. 5. Peak Ground Acceleration (PGA) and Arias Intensity for each shake of the ground motion sequence.

Table 3 Measured shear wave velocities and calculated G_{max} for test #1.

		V _s (m/s)		G _{max} (MPa)	
Depth		100A	25ABCD	100A	25ABCD
Shallow($\sigma'_v \sim$ 45 kPa)	Pre-shake	158	164	48	57
	Post-shake	146	154	41	50
Deep(σ' _v ~90 kPa)	Pre-shake	164	199	51	84
	Post-shake	167	195	54	80

amplitude, (2) constant amplitude at a target peak acceleration, and (3) an exponential decay of amplitude. The design of the waveform topology was to mimic the distribution of energy in a recorded earthquake motion and match the typical s-shape of a Husid plot [19]. Matching the shape of a Husid plot is a similar approach used to create artificial accelerograms containing complex frequencies [20]. The synthetic input motion does not include complex frequencies or near-fault effects unique to an individual ground motion record. A single frequency input motion reduces the uncertainty of experimental findings and is common in centrifuge testing [9,15]. In Fig. 4, the waveform phases are identified with different shadings using the recorded input motion from shake 3. Provided in Table 2 is the number of cycles during each shaking phase for the ground motion sequence.

The shaking magnitude and number of cycles of each shake were chosen to elucidate specific system-level mechanisms and behaviors. Specifically, shake 1 was used to estimate elastic properties, shake 2 to trigger liquefaction, shake 3 to induce cyclic mobility following liquefaction triggering, and shake 4 to produce large embankment deformations. The achieved Peak Ground Accelerations (PGAs) and Arias Intensities (I_a) for both tests are given in Fig. 5. Adequate time was provided between shaking events for excess porewater pressures to fully dissipate before the next shake in the sequence.

2.2. In-situ measurements and monitoring

The embankment in-situ instrumentation consisted of vertical arrays of porewater pressure transducers and accelerometers located beneath the level ground above the slope and in the mid-slope. A 5 cm vertical

spacing between accelerometers was selected to sufficiently measure high frequencies, required for inverse analysis procedures to interpret shear wave transmission. Using the expression of $f_{\text{max}} = V_{\text{s}}/(8 \cdot \Delta Z_{\text{max}})$ by Kamai and Boulanger [21], the highest frequency (fmax) was estimated for a given shear wave velocity (V_s), and vertical spacing between adjacent accelerometers (ΔZ_{max}). With the 5 cm sensor spacing and assuming the shear wave velocity of the liquefied soil was 20 m/s, the maximum measurable frequency was 50 Hz, which was higher than the 40 Hz input motion (model scale). Located at the midpoint between adjacent accelerometers were porewater pressure transducers. The porewater pressure transducers were vertically spaced 5 cm; however, they were placed 6 cm out-of-plane from the accelerometers towards the center dividing wall for additional spacing between sensors. The level and sloping ground sensor arrays had similar sensor types at equivalent depths from the ground surface (e.g., the depth to P5 and P9 is the same) and, therefore, had comparable initial vertical effective stresses. Thus, measured differences in dynamic behaviors between the level ground and mid-slope arrays are attributed to the initial static stress produced by the 10-degree slope.

Bender elements were used to measure shear wave velocities to estimate small-strain stiffnesses (maximum shear modulus $G_{max})$ in each embankment before and following shaking. Shear wave velocities were measured at two depths beneath the level ground above the slope. Table 3 lists the V_s measurements and the calculated G_{max} for test #1. G_{max} was calculated using the expression, $G_{max} = \rho V_s^{\ 2}$, wherein the mass density ρ was taken as the specified saturated mass density at $D_r = 63\%$ ($\rho_{100A} = 1958 \ kg/m^3$ and $\rho_{25ABCD} = 2154 \ kg/m^3$). The average calculated G_{max} in the 25ABCD soil was about 40% larger than in the 100A soil and is a product of the higher shear wave velocities and saturated density. Shear wave velocity data was unavailable for test #2 due to a malfunctioned amplifier.

The one-dimensional fundamental period of a uniform soil column is expressed by $F_0=4D/V_s$, where D is the depth of the soil layer. The embankments cannot be described by a single fundamental frequency due to the varying depths (D) and increases of V_s with depth. A range of fundamental frequencies can be estimated assuming a uniform V_s and considering depths of the level ground above and below the slope. For test #1, assuming an average pre-shake V_s of 161 and 182 m/s produces an F_0 range of \sim 2.9–5 Hz and 3.3–5.7 Hz for the embankments #1A and

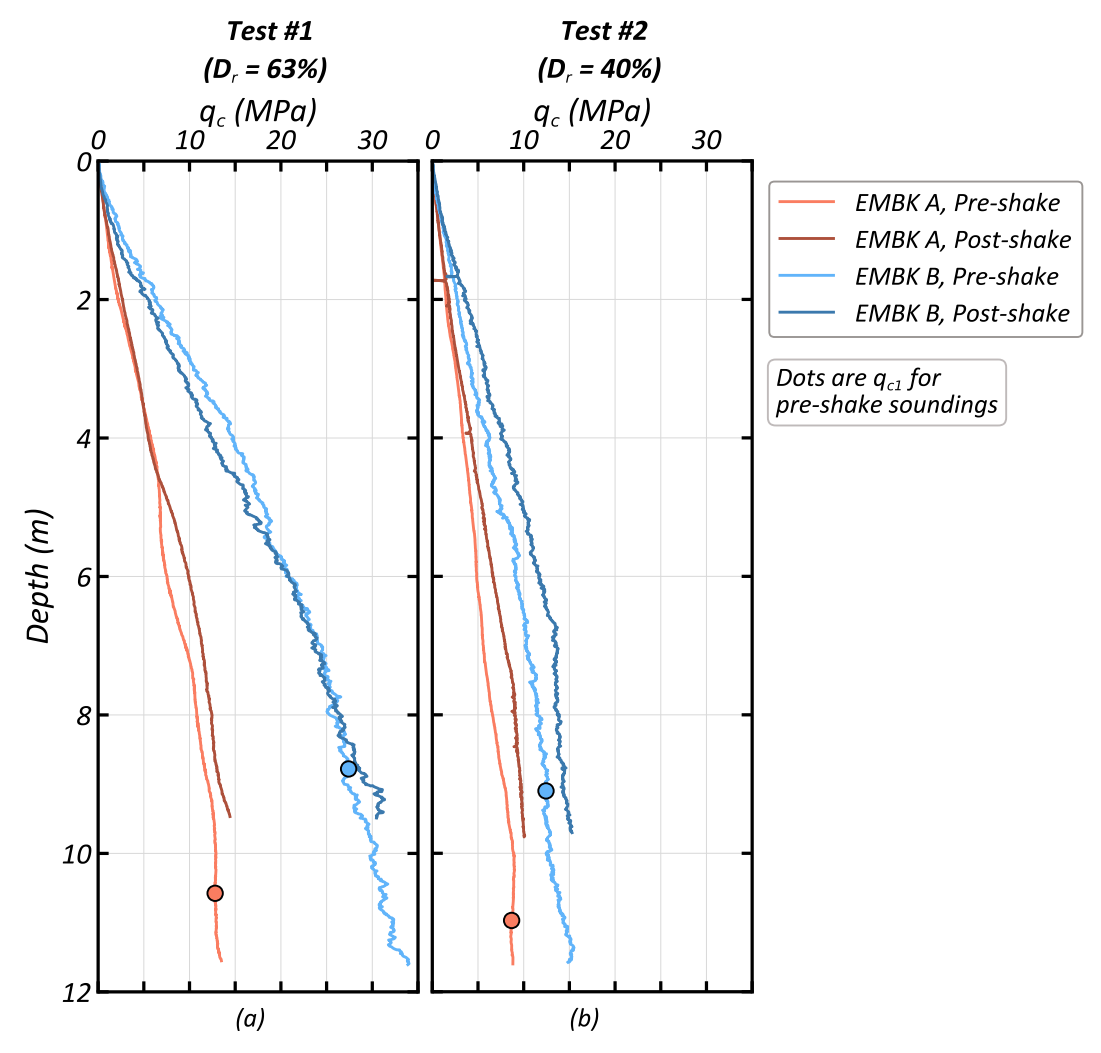


Fig. 6. Pre- and post-shake CPT profiles for (a) test #1 and (b) test #2.

#1B, respectively. The similar ranges of fundamental frequencies imply that the amplification of the input motion and the associated imposed seismic demand will be similar for the first shake (i.e., elastic strain level) for each embankment.

Cone penetration tests (CPTs) were used to characterize the initial, final, and change of soil conditions from strong shaking. The locations of the CPT soundings are labeled in Fig. 3b. The post-shake CPTs were pushed following the completion of the ground motion sequence. The CPT device was designed at the UC Davis CGM [16,22,23] and consisted of a 10 mm diameter penetrometer to minimize particle-to-probe effects in the 25ABCD soil. The D_{CPT}/D_{85} of the 10 mm CPT for the 100A and 25ABCD sands is 37 and 4.1, respectively. Pires-Sturm and DeJong [24] noted that a D_{CPT}/D_{85} less than $\sim\!5$ will produce elevated tip resistance (qc), and using their relationship, the increase in qc for the 25ABCD soil is a factor of $\sim\!1.2$. The CPTs were pushed into the soil for 457 mm (18") at a penetration rate of 1 cm/s using a hydraulic actuator.

Fig. 6 presents the CPT profiles for both tests. The dots on the preshake soundings represent the depth where the vertical effective stress is equal to 1 atm (q_{c1}) for the specific sand and relative density. The preshake q_{c1} for embankment #1B was about 2.2 times larger than the q_{c1} measured in embankment #1A (Fig. 6a). The larger q_{c1} in the 25ABCD sand is linked to the lower void ratio range compared to the 100A sand. Pires-Sturm and DeJong [24] noted that as e_{min} and e_{max} decrease, q_{c1} is expected to increase due to larger G_{max} and higher peak shear strengths. The post-shaking CPT profiles for both embankments were similar to the pre-shaking profiles. This suggests that only minimal densification

occurred during reconsolidation following liquefaction. In test #2 (Fig. 6b), the difference of q_{c1} decreases to a factor of $\sim\!1.6$, indicating relative differences of q_{c1} were density dependent for these soils. The post-shaking CPT profiles show an increase in cone tip resistance in both embankments, suggesting densification during post-liquefaction reconsolidation was more significant for test #2.

2.3. Ex-situ boundary tracking

Contact sensors are the traditional method for measuring displacing soil in centrifuge experiments [25-27]. It has been observed that the soil where contact sensors were touching can become reinforced and have elevated liquefaction resistance compared with the surrounding soil [28]. Instrument racks used to mount contact sensors above soil surfaces may also limit access for other measurements or instruments [26]. Other researchers have overcome the drawbacks of contact sensors by positioning highspeed cameras above model containers and using image analysis software to track the movement of soil or markers during liquefaction [29–31]. Mounting cameras above the specimen container was not feasible for the experiment described herein due to the physical length of the model container and the use of a model container lid required for safe operation during testing. This led to developing an ex-situ camera hardware configuration novel to the CGM. The longitudinal sidewalls of the model container were clear polycarbonate and acted as windows allowing for a plane-strain cross-sectional view of the embankment geometries. Highspeed cameras were positioned adjacent

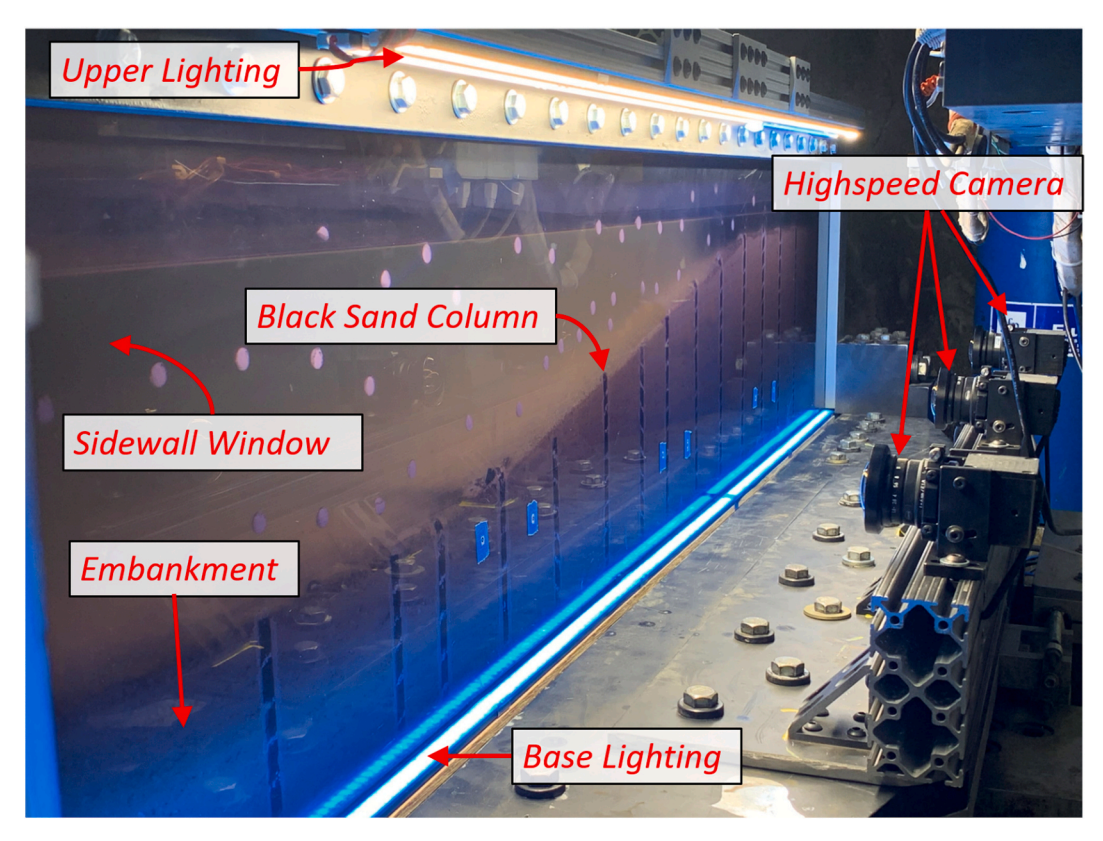


Fig. 7. Image of ex-situ highspeed camera configuration used to record cross-sectional slope displacements. (Shown for embankment #2A).

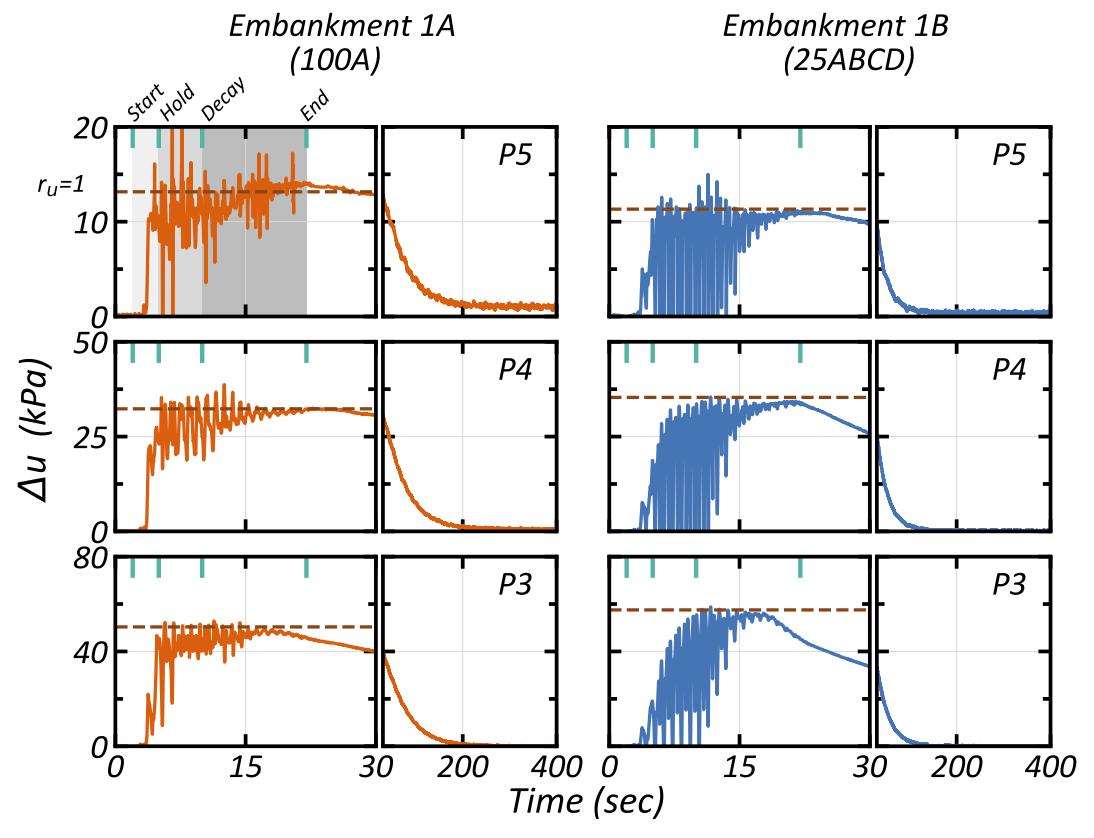


Fig. 8. Excess porewater pressure response of the level ground condition (P3, P4, and P5) for test #1.

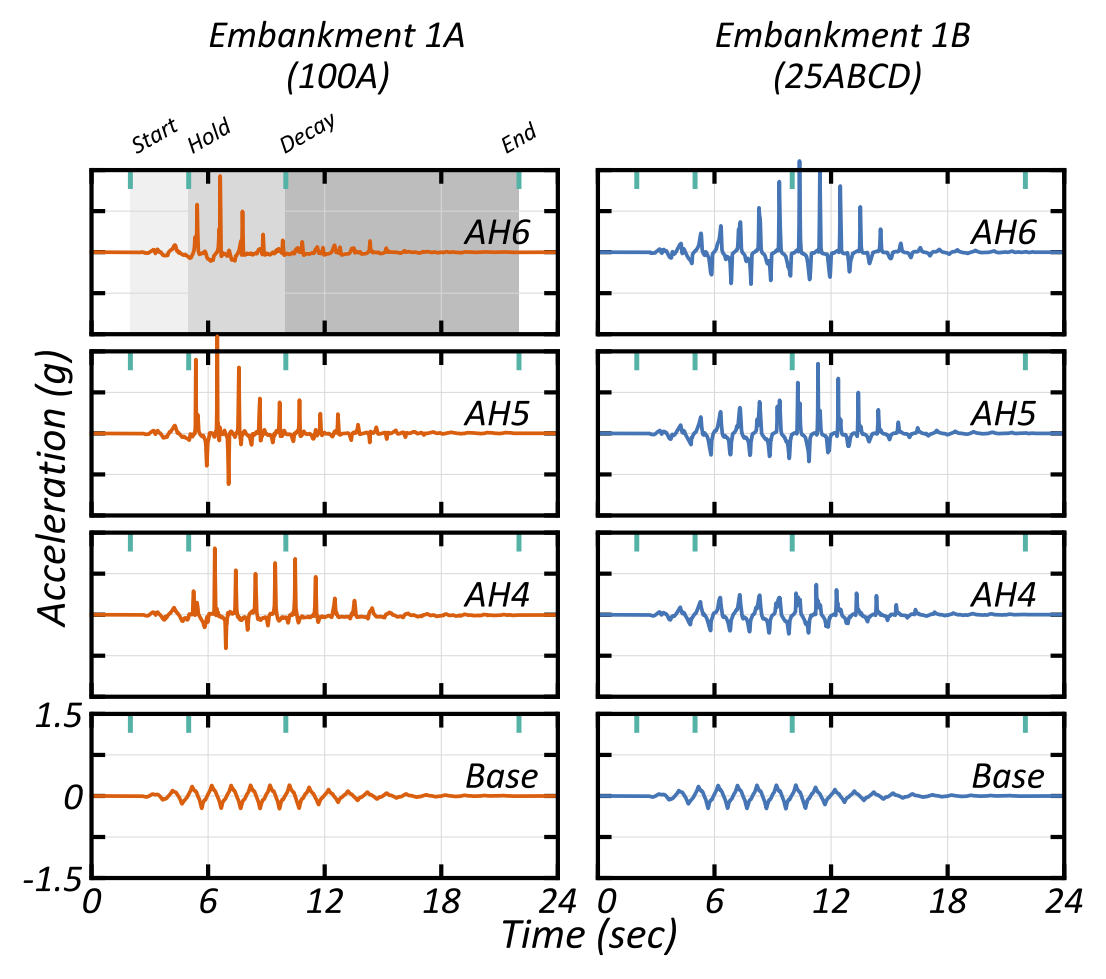


Fig. 9. Acceleration response of the level ground condition (Base, AH4, AH5, and AH6 for test #1). The base motion is identical in both columns.

to the longitudinal windows and recorded the deforming embankments during liquefaction. The videos were converted to displacement time histories using GEOPIV-RG [32,33], which has a strong track record of use for geotechnical engineering applications [34–37]. In previous studies using cameras to record cross-sectional deformations of soil through transparent windows, interface friction along the windows was identified to cause local deformations that differed from free-field locations [38,39]. Hand measurement surveys following testing did not indicate the deformations were different near the windows.

Three high-speed cameras were positioned along the length of each embankment about 310 mm from the window. This was the maximum distance possible due to space constraints between the model container and centrifuge bucket. Fig. 7 shows a labeled photo of the configuration of the camera setup that was typical for both tests. The key components of the camera configuration include.

- Sidewall windows: Each window was polished on both sides to improve optical clarity to remove fine scratches that cause blurry images and diffuse light.
- Lighting: A LED light bar that provided 8000 lumens of indirect light was attached to the lid of the model container and is labeled as 'upper lighting' in Fig. 7. The base lighting was added before test #2 for an additional 5500 lumens.
- Cameras: Photron FASTCAM MH6s were used. The FASTCAM system
 consists of 6 cameras equipped with Kowa 6 mm lenses and are
 controlled by a central computer. A central computer enabled time
 synchronized recording of the cameras, and recording was automatically initiated using the data acquisition system that sampled insitu sensors. This established a known time correlation between the

- cameras and in-situ sensor measurements. Each camera was recorded at 1000 frames per second at a 1280x1080 px resolution and was rigidly attached to the centrifuge shake table. Therefore, embankment movements during liquefaction were relative to the container and cameras. Lens distortion effects were corrected using a built-in function within the Photron capture software.
- Black sand columns: Black sand columns were added to visualize embankment deformations. The columns were designed to move with the embankments and be minimally invasive during model construction. The columns were created by mixing dyed sand with water-soluble glue, pressing the glue sand mixture into a mold, and letting the mixture dry. The dried columns were attached to the windows using more sand and water-soluble glue, enabling dissolution during saturation. Several columns were extended beyond the top of the soil surface to confirm the glue did not provide reinforcement. The columns fell apart once the glue softened during saturation.

The sand was too uniform in color for GEOPIV-RG to accurately track movements at the camera resolution and position from the model container windows. However, the high contrast of the black sand columns was easily tracked by GEOPIV-RG, and the displacements presented herein are of those columns. Additional columns were added in test #2 to provide better resolution of displacement patterns.

GEOPIV-RG tracks soil position by dividing an image into a mesh of patches and tracking the translation of each patch from a user-defined reference point. A custom mesh of 60 px diameter patches was defined for each black sand column. The patches were spaced 20 px apart to ensure full coverage. To verify GEOPIV-RG accurately measured the

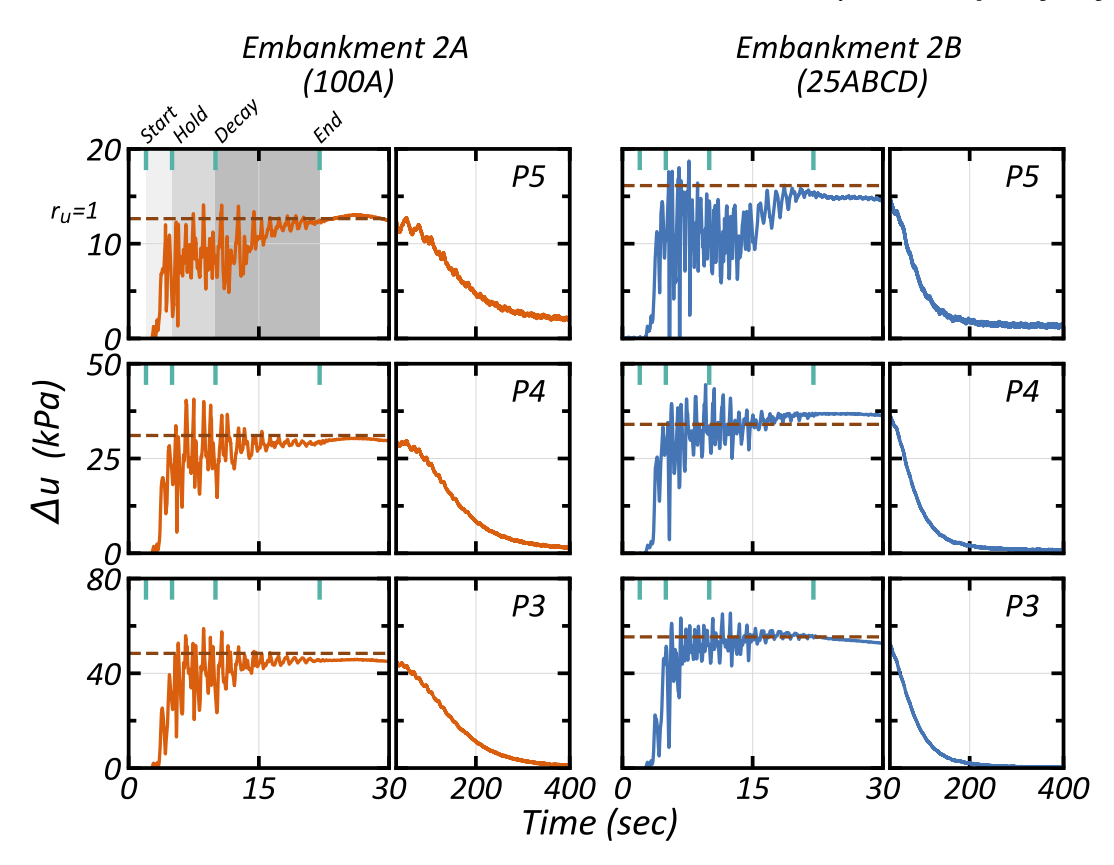


Fig. 10. Excess porewater pressure response of the level ground condition (P3, P4, and P5) for test #2.

black sand column positions, patch locations were superimposed on the original camera images to check for fit. The GEOPIV analysis was performed using the Eulerian analysis mode.

The raw output from GEOPIV is displacement time histories in units of pixels. To convert pixels to engineering units (mm), the camera configuration used in the experiment (i.e., camera spacing, focal length, and image size) was replicated in the laboratory, and images were taken of a calibration checkerboard taped on the inside of the empty model container window where the soil would be. The number of pixels that spanned the known size of the checkers was counted at each black sand column location to find the pixel to mm scale factor. The typical scale factors ranged from 3.1 to 3.2 px/mm (12.4–12.8 px/cm prototype).

3. Test results

The in-situ dynamic behavior of the tests is compared using acceleration traces and excess porewater pressure responses for the sensor arrays located beneath the level and sloping ground. Liquefaction-induced deformations of the embankments are compared using results from the highspeed cameras and the GEOPIV-RG image analysis procedure. Results are given for shake 3 (Fig. 4), which was selected since significant excess porewater pressures were measured in each test, resulting in cyclic mobility following liquefaction triggering. The other shakes in the ground motion sequence exhibit similar trends as shake 3 but are not shown for the sake of brevity. Results from the other shakes are summarized in CGM data reports [40,41]. All measurements and units are provided in prototype scale unless noted otherwise.

3.1. Level ground conditions (LGC)

LGC: Test #1 Fig. 8 presents the excess porewater pressure response for the P3, P4, and P5 transducers for embankments 1A and 1B. Fig. 8 has a split time scale to show the generation and dissipation of excess porewater pressures (Δu). The dashed lines in the 0–30 s frames indicate the Δu that is equal to the initial vertical effective stress and therefore identifies when liquefaction is triggered following the excess porewater pressure ratio ($r_u=1.0$) criterion [42]. The green tick marks in the figures (labeled in the top left cell) denote the beginning of the input motion, the constant amplitude cycles, exponential decay cycles, and the end of the motion. This labeling is consistent throughout the figures herein.

Excess porewater pressures accumulated at a slower rate and dissipated faster at P4 and P3 in embankment 1B for the two embankments in test #1. The slower generation of excess porewater pressures for P4 and P3 in embankment 1B delayed the initial triggering of liquefaction ($r_{\rm u}=1$), which did not occur until the cyclic amplitude of the input motion began to decay at 9 s. In contrast, excess porewater pressures at P4 and P3 in embankment 1A reached a $r_{\rm u}$ of 1.0 at the beginning of the constant amplitude cycles. To characterize differences in dissipation times during upward seepage following shaking, the time for 50% of excess porewater pressures to dissipate (t_{50}) was calculated for each sensor. For embankment 1B, the t_{50} times were 18.3 and 18.7 s for P4 and P3 compared with 43.1 and 37.9 s for the same sensors in embankment 1A. The slower generation and faster dissipation times occurred despite the 25ABCD soil having a lower initial permeability ($t_{25ABCD}=0.011\ tm/s$ and $t_{100A}=0.021\ tm/s$).

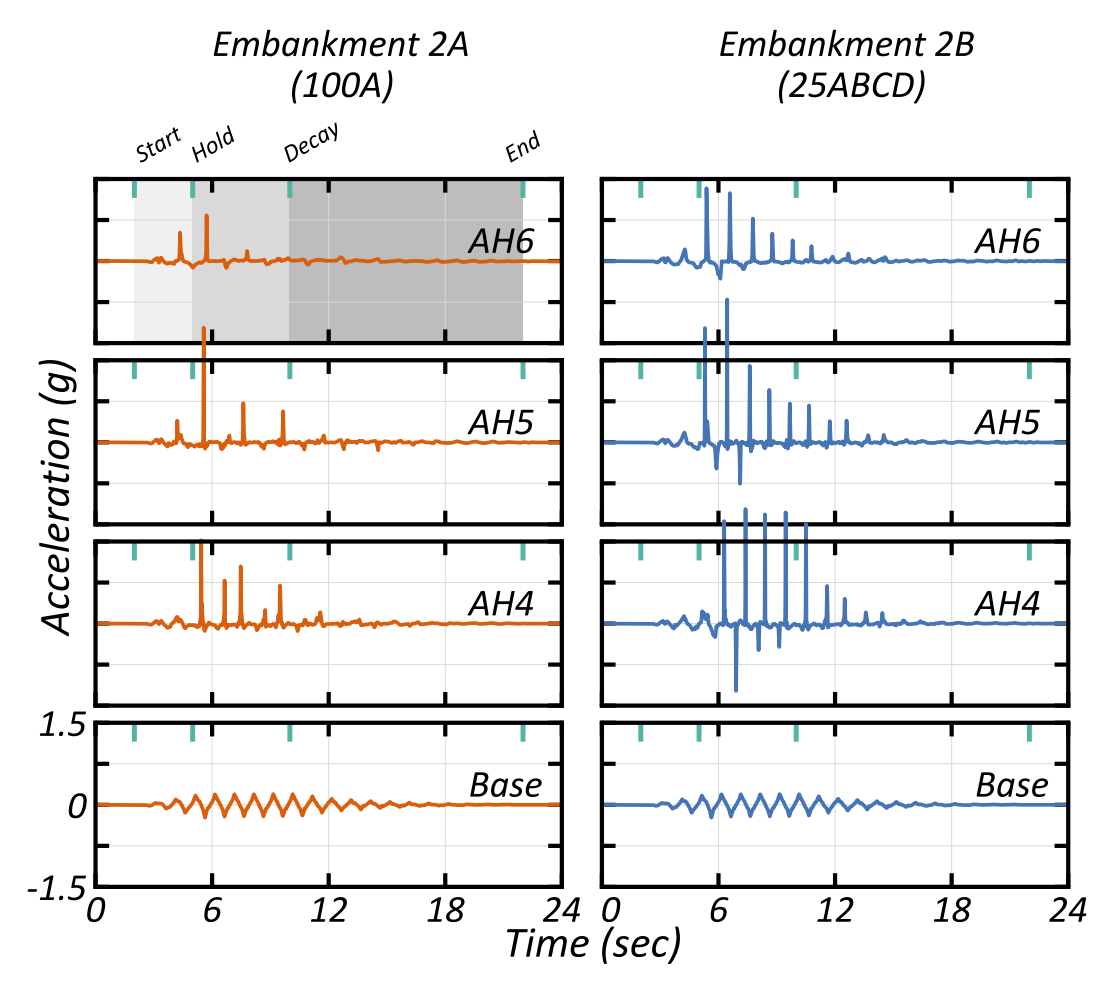


Fig. 11. Acceleration response of the level ground condition (Base, AH4, AH5, and AH6) for test #2.

More frequent and larger magnitude drops in excess porewater pressures occurred in embankment 1B during shaking. The drops in excess porewater pressure occurred as the soil dilated following phase transformation from a contractive to a dilative state. The dilation spikes in the excess porewater pressure response reduced $r_{\rm u}$ less than 1.0, momentarily causing the soil to deliquefy [43]. The drops occur at a frequency of 0.5 Hz in embankment 1B. This suggests that dilation occurs during up- and down-slope accelerations of the input motion (i.e., 2x per cycle). Dilation spikes were less frequent in embankment 1A and only occur during the downslope acceleration cycles (i.e., positive acceleration) at the input motion frequency of 1 Hz. The spikes indicate that embankment 1B exhibits stronger dilatancy, critical for resisting embankment instability following liquefaction triggering.

The acceleration response for AH4, AH5, AH6, and the recorded model container motion is provided in Fig. 9. The sharp pulses of acceleration are related to the same dilation behavior in the excess porewater pressure response and are an additional indicator that liquefaction was triggered. The dilative response during loading transforms the upward propagating shear waves into a sharp wavefront, causing an acceleration pulse [43]. For embankment 1B in Fig. 9, more frequent spikes occurred, which is consistent with the excess porewater pressure response in Fig. 8. The occurrence of dilation spikes does vary with depth across embankments 1A and 1B, reflecting the different degrees of liquefaction and excess porewater pressure evolution. Specifically, at

the AH4 accelerometer depth, liquefaction was triggered in embankment 1A (see P3 Fig. 8), but liquefaction was not triggered in embankment 1B until later in the motion.

LGC: Test #2 The excess porewater pressure response for P3, P4, and P5 for test #2 is provided in Fig. 10. Liquefaction was triggered at about 5 s at all transducers in both embankments. The porewater pressure response during shaking (0-30 s) is similar in both embankments. The dissipation of excess porewater pressures in embankment 2B is faster than embankment 2A, which is consistent with the findings from test #1 (Fig. 8). The t_{50} times measured from the end of shaking for P5, P4, and P3 for the embankments 2A and 2B are 146, 129, 117 and 59, 55, 50 s, respectively.

The acceleration response for AH4, AH5, and AH6 for test #2 is provided in Fig. 11. The recorded motion at each accelerometer was significantly transformed from the original input motion in both embankments. The soil at AH5 and AH6 in embankment 2A had a complete loss of stiffness, and upward propagating shear waves were intransmissible except for several dilation spikes early in the shake. The 25ABCD soil in embankment 2B maintained enough structure and stiffness to transmit shear stresses throughout the array. Six distinct dilation peaks for AH6 are visible from 5.5 to 10.5 s in embankment 2B, consistent with the input motion frequency.

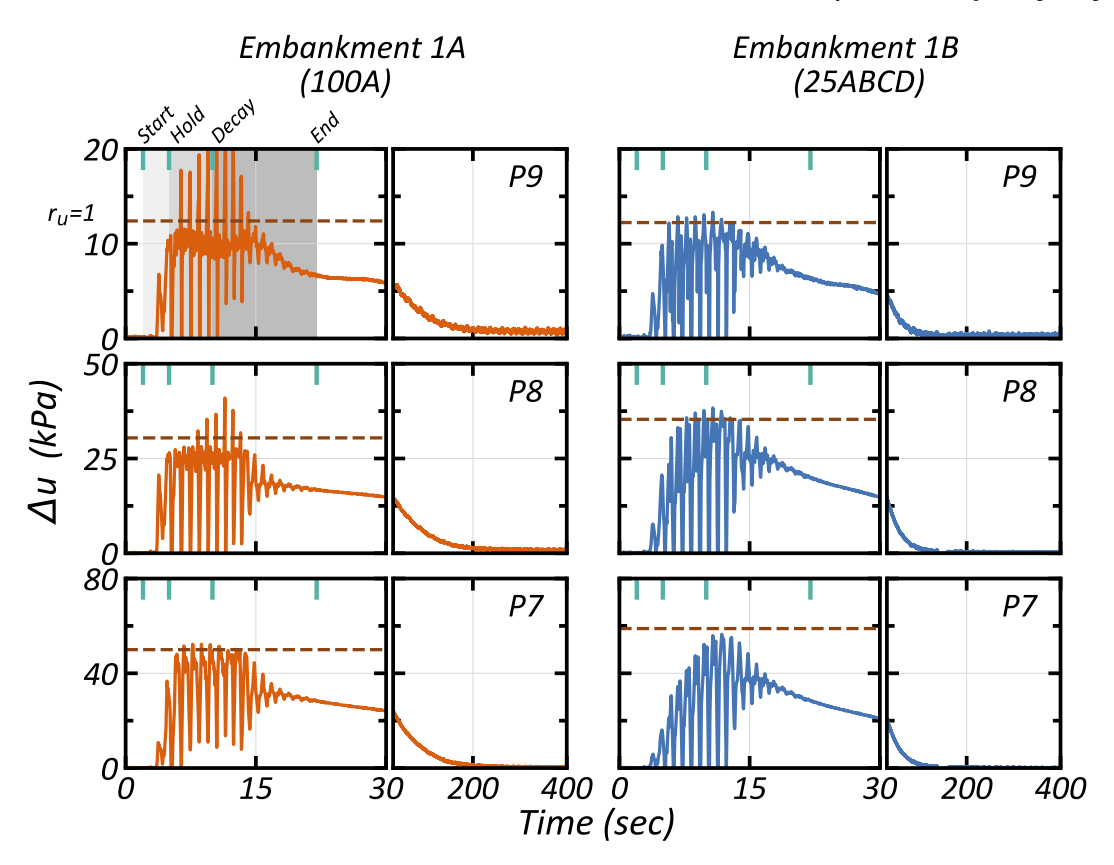


Fig. 12. Excess porewater pressure response of the sloping ground condition (P7, P8, and P9) for test #1.

3.2. Sloping ground conditions (SGC)

The 10-degree slope induces a minor initial static shear stress on the soil that will modify cyclic behavior. The impact of the static shear stress varies with sand gradation, stress conditions, and relative density [42]. To measure the influence from static shear stress, the sensor array within the slope was identical to the array located beneath the level ground in terms of sensor spacing, overburden stresses, and position from the longitudinal walls. Therefore, measured differences in dynamic behavior between the two arrays are attributed to the static shear stress.

SGC: Test #1 The excess porewater pressure response for P7, P8, and P9 for test #2 is provided in Fig. 12. Embankment 1B had increased liquefaction resistance compared with embankment 1A, exhibited by the additional number of cycles required to reach a $r_u = 1.0$. Compared with the level ground conditions in Fig. 8, embankment 1A had a more pronounced dilative response.

Elevated excess porewater pressures are not maintained at any of the sensor locations in either embankment for the duration of the input motion, and pressures dissipated to about half of the peak values when shaking ended. Embankment 1B dissipated excess porewater pressures more rapidly than embankment 1A.

The acceleration response for AH9, AH10, and AH11 for test #1 is given in Fig. 13. Larger magnitude dilation spikes were measured in the sloping ground than the level ground. The dilation spikes are consistent with the excess porewater pressure response in Fig. 12. The dilation spikes are larger in embankment 1A, possibly because dilatancy may not have been fully mobilized in embankment 1B since liquefaction occurred later in the motion.

SGC: Test #2 The pore pressure response for P7, P8, and P9 for test

#2 is provided in Fig. 14. Liquefaction was triggered in both embankments in 1–2 cycles. In embankment 2A, a steady upper limit of excess porewater pressures (corresponding to a $r_u=1.0$) was maintained at P7 and P8 until roughly 15 s. The amplitude of the input motion decreased after 15 s, and excess porewater pressures began to dissipate. The constant excess porewater pressures at P7 and P8 in embankment 2A following shaking are caused by upward seepage from the underlying soil during reconsolidation. In contrast, in embankment 2B excess porewater pressures at P7 and P8 decreased immediately, suggesting upward seepage was not constant.

The acceleration response for AH9, AH10, and AH11 for test #2 is provided in Fig. 15. Both embankments have about the same number of dilation spikes; however, the spikes in embankment 2B are larger in magnitude and occur with the frequency of the 1 Hz input motion.

3.3. Embankment displacement

The acceleration and excess porewater pressure responses in Figs. 8–15 indicate that liquefaction was triggered in all four embankments. Understanding the effect soil gradation has on liquefaction-induced embankment deformations is required to better account for gradation properties in liquefaction analysis procedures. Improving the knowledge of how deformation response is related to soil gradation is represented in this work by the 100A and 25ABCD sands.

In Figs. 16 and 17, the horizontal and vertical displacements of the black sand columns for both tests are shown with the embankment geometry. The displacement fields in the figures are magnified 10 times and only provide the displacements incurred during shake 3. The black sand columns deform over the height of the embankments but could not

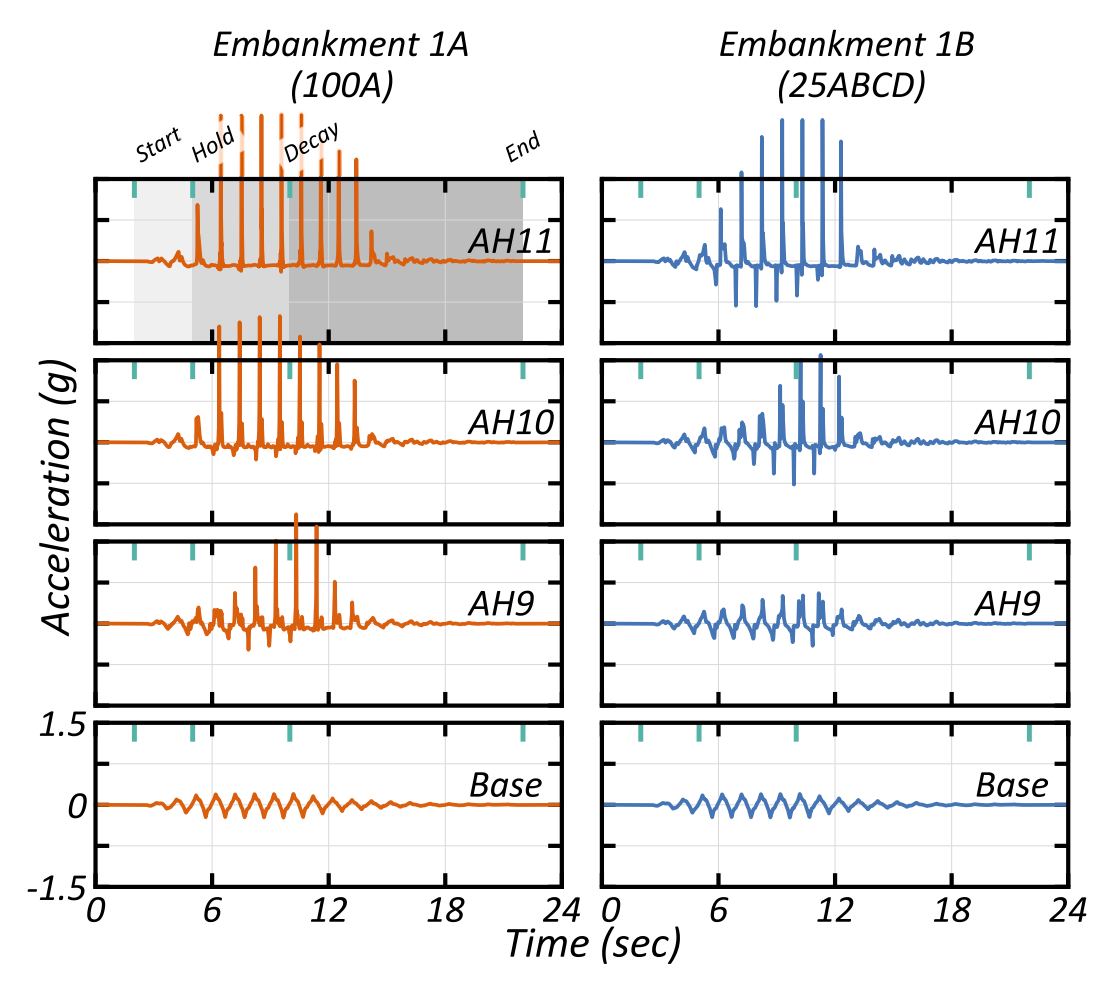


Fig. 13. Acceleration response of the sloping ground condition (Base, AH9, AH10, and AH11) for test #1.

be recorded with the highspeed cameras below a height of 5 m.

Test #1. Displacements of larger magnitudes and to greater depths were measured in embankment 1A. The deformations are consistent with the excess porewater pressure and acceleration measurements that indicated rapid triggering of liquefaction and prolonged embankment instability from elevated excess porewater pressures. The slope surface horizontal and vertical displacements at mid-slope (horizontal distance of 34 m) of embankment 1A was roughly 0.3 m and 0.01 m, respectively.

Embankment 1B only incurred minor deformations during shaking, which is consistent with the dilative behaviors in the acceleration and excess porewater pressure measurements. At larger depths below the ground surface, only minimal displacement occurred. The mid-slope surface, horizontal and vertical displacements were 0.08 m and 0.01 m, respectively.

Test #2. Large magnitudes of displacements were recorded over the entire height of embankment 2A. Except for the black sand columns in the upslope level ground conditions, displacements extended past the 5 m cutoff. The magnitude and extent of displacements are consistent with the recorded responses from in-situ sensors. The mid-slope surface horizontal and vertical displacements were 0.85 m and 0.1 m.

Embankment 2B had a similar pattern of displacements as embankment 2A, but the deformations were lower. The stronger dilatancy in the 25ABCD sand is one of the factors that may have aided in curtailing downslope displacements during cyclic mobility. The mid-slope surface horizontal and vertical displacements were 0.33 m and 0.01 m.

4. Conclusions

A centrifuge testing program was performed that evaluated the effects of sand gradation, as represented in this work by the 100A and 25ABCD sands, on the dynamic performance of embankments during liquefaction. The centrifuge experiment consisted of two submerged embankments with uniform soil profiles positioned side-by-side in the same model container. The soils used to construct the embankments were a poorly graded and well graded sand, and were dry pluviated to the same relative density. The shaking sequence used to trigger liquefaction consisted of four, 1 Hz motions with increasing seismic energy with successive events. The testing program consisted of two centrifuge experiments, with the only difference between the experiments being the relative density of the embankments. The test densities for tests 1 and 2 were $D_{\rm r}=63\%$ and $D_{\rm r}=40\%$.

Novel hardware and measurement techniques were developed to characterize the embankment dynamic performance and deformation response during shaking. These contributions are as follows:

 Testing two embankments in the same model container reduced the variability from four different input container motions. The achieved input motions for the two experiments were almost identical, which allowed for the comparison of test results. Positioning the embankments parallel to each other produced a more direct comparison of the dynamic behaviors.

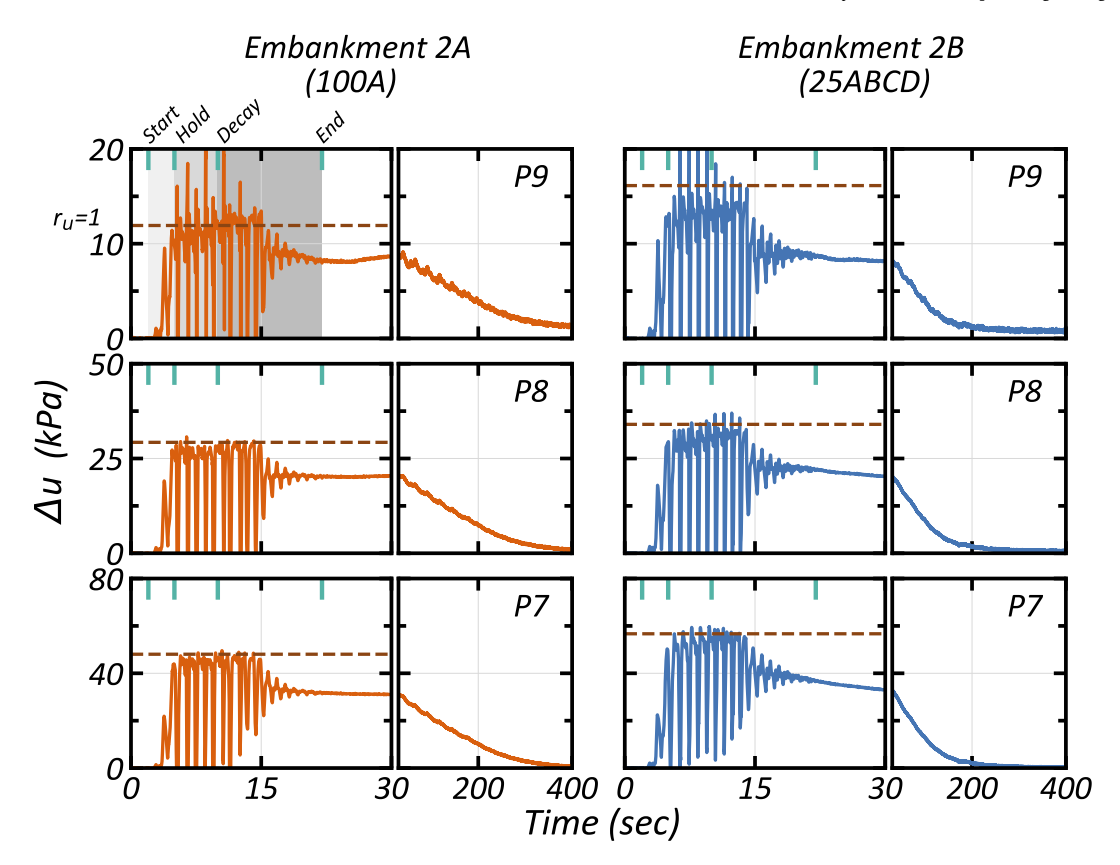


Fig. 14. Excess porewater pressure response of the sloping ground condition (P7, P8, and P9) for test #2.

- The high-speed camera and lighting configuration developed for the CGM produced clear, high contrast photos of the deforming embankment cross-sections by recording through the transparent model container sidewalls. The use of three cameras to record each embankment during strong shaking allowed for recording over the entire embankment length. This advanced beyond the standard approach of recording a centrifuge model cross-section using a single camera. Camera recordings of the movement were converted to images, and cross-sectional liquefaction-induced displacement time histories were created using GEOPIV-RG image analysis software.
- The dyed columns of sand provided sufficient contrast for accurate GEOPIV-RG position tracking during strong shaking. The columns were fabricated and attached to the model container windows using water-soluble glue. Attaching the columns to the model container prior to embankment construction avoided creating loose or disturbed pockets of sand if the columns were installed following construction.

The following are the main observations of sand gradation effects on embankment performance:

- The 25ABCD sand had a larger initial shear modulus due to larger absolute density and measured shear wave velocities.
- \bullet The CPT cone tip resistance at q_{c1} for the well graded sand can be significantly higher than the cone-tip resistance for the poorly graded sand at the same relative density. The relative difference of q_{c1} for the two test sand gradations was larger for test #1 (Dr =63%), suggesting that changes in relative differences in cone tip measurements are variable with density.
- The well graded 25ABCD sand better transmitted transient shear stresses to the ground surface than the 100A sand following liquefaction triggering. The shape of the input motion was not attenuated as much in embankments 1B and 2B. This suggests the 25ABCD sand

- better maintained shear stiffness following the initial onset of liquefaction.
- The well graded 25ABCD sand had greater resistance to the generation and faster dissipation of excess porewater pressures despite
 having lower permeability. This reduced the time of sustained excess
 porewater pressures in the 25ABCD embankment.
- In the individual tests, the liquefaction-induced deformations were lower in the embankments constructed with a well graded sand. While the poorly graded sand embankments had larger deformations, they did exhibit similar deformation patterns as the well graded sand embankments.
- The performance of the side-by-side 100A and 25ABCD embankments was notably different in both tests, even though the embankments were prepared to the same relative densities. This demonstrates that the current body of knowledge and engineering procedures pertaining to liquefaction evaluations is incomplete and suggests that additional factors such as initial void ratio, shear stiffness, and soil gradation should be considered more explicitly.

Credit author statements

Trevor Carey: Conceptualization, Methodology, Investigation, Formal analysis, Software, Writing – Original Draft, Visualization. Anna Chiaradonna: Investigation, Methodology, Writing - Review & Editing. Nathan C. Love: Investigation, Methodology, Software, Formal analysis, Writing - Review & Editing. Daniel W. Wilson: Conceptualization, Methodology, Writing - Review & Editing. Katerina Ziotopoulou: Conceptualization, Methodology, Supervision, funding acquisition, Writing - Review & Editing, Project administration. Alejandro Martinez: Conceptualization, Methodology, Supervision, funding acquisition, Writing - Review & Editing, Project administration. Jason T. DeJong: Conceptualization, Methodology, Supervision, funding acquisition, Writing - Review & Editing, Project administration.

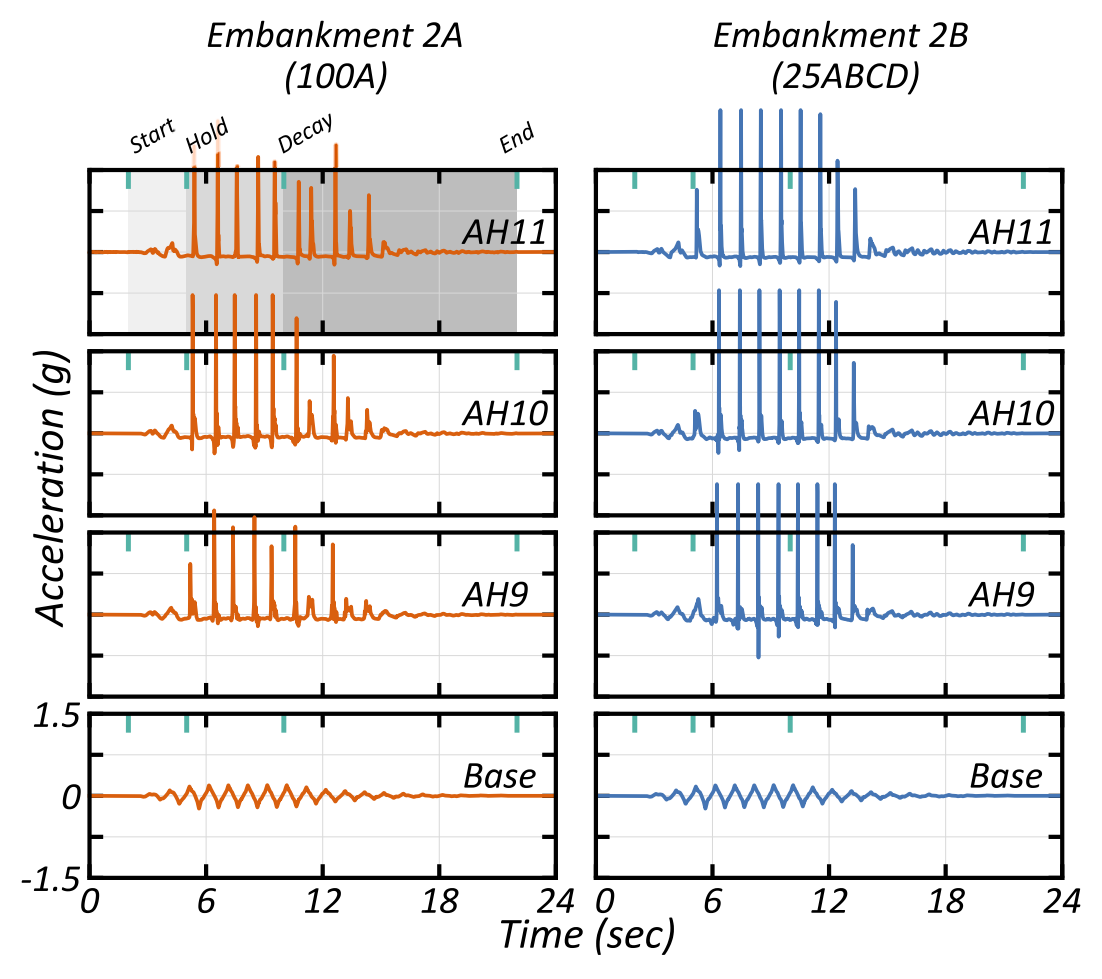


Fig. 15. Acceleration response of the sloping ground condition (Base, AH9, AH10, and AH11) for test #2.

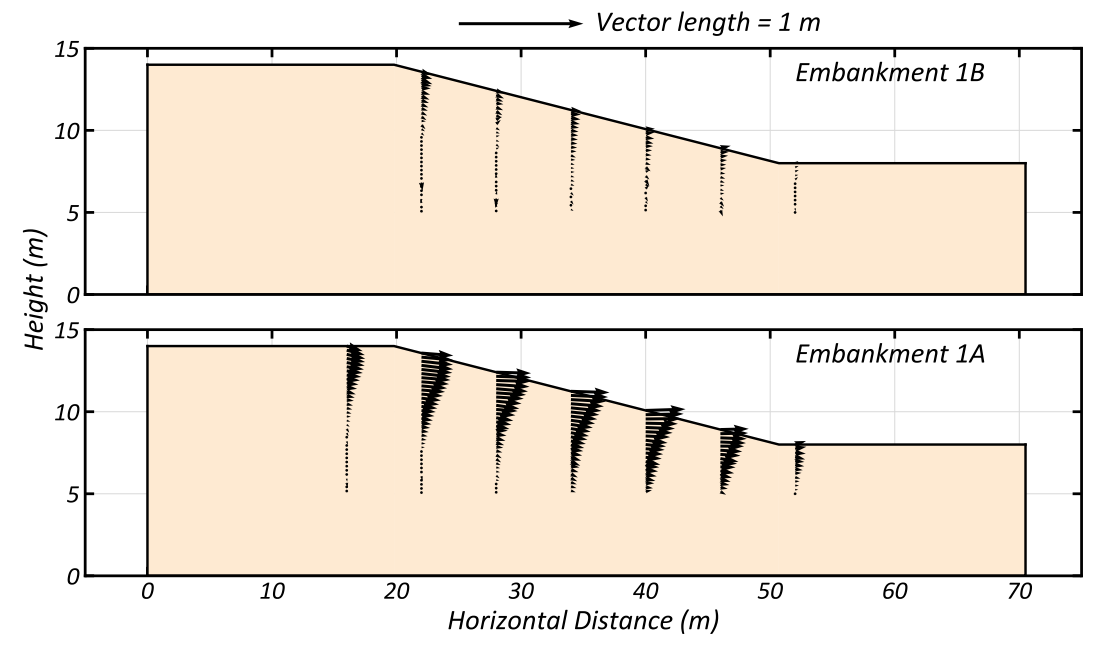


Fig. 16. 10x magnified slope displacements incurred during shake 3 for test #1. The vector given above the figure corrsponds to 1 m of displacement.

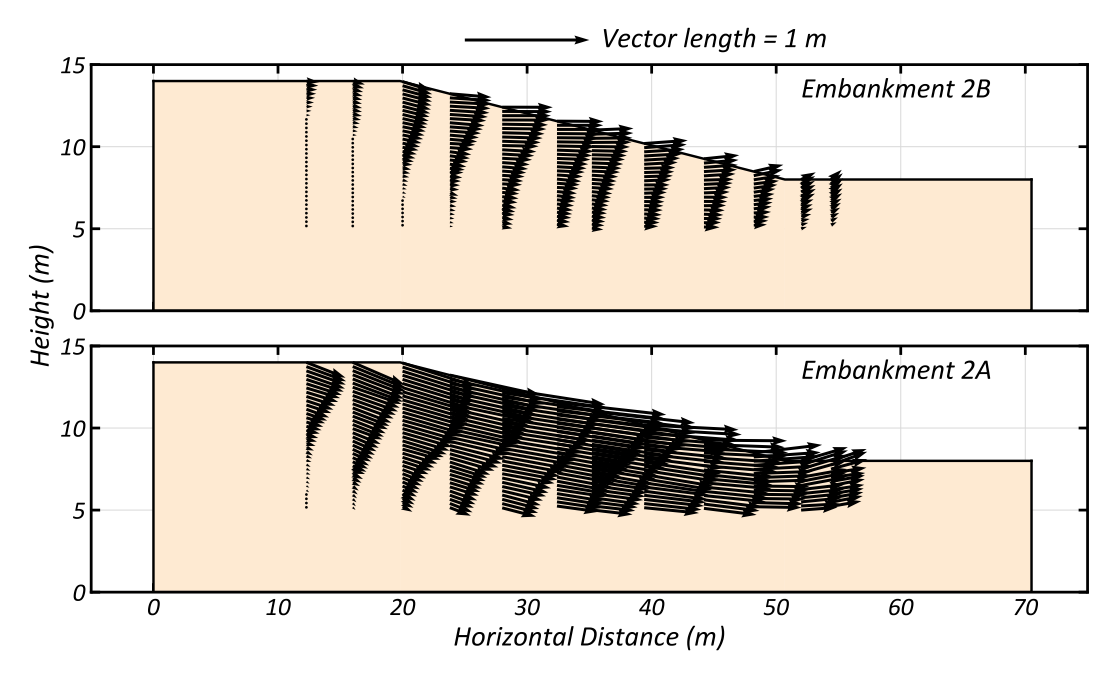


Fig. 17. 10x magnified slope displacements incurred during shake 3 for test #2. The vector given above the figure corrsponds to 1 m of displacement.

Declaration of competing interest

The authors declare that they have no known competing financial interests or personal relationships that could have appeared to influence the work reported in this paper.

Acknowledgments

The National Science Foundation (NSF) provided the funding for this work under grant No. CMMI-1916152 and also funded the Natural Hazards Engineering Research Infrastructure (NHERI) shared use centrifuge facility at the University of California at Davis under grant No. CMMI-1520581. Additional support was provided by the Fulbright Scholar Program. The authors would also like to thank Rachel Reardon, Francisco Humire, Mandeep Singh Basson, and Sheikh Sharif Ahmed, for their insights and recommendations. The assistance of the staff at the UC Davis CGM is also gratefully acknowledged.

References

- Seed HB, Idriss IM, Lee KL, Makdisi FI. Dynamic analysis of the slide in the lower san fernando dam during the earthquake of february 9, 1971. J Geotech Eng Div 1975;101(9):889–911.
- [2] Ishihara K, Koga Y. Case studies of liquefaction in the 1964 Niigata earthquake. Soils Found 1981;21(3):35–52.
- [3] Boulanger RW, Mejia LH, Idriss IM. Liquefaction at moss landing during loma prieta earthquake. J Geotech Geoenviron Eng 1997;123(5):453–67.
- [4] Ishihara K. Liquefaction and flow failure during earthquakes. Geotechnique 1993; 43(3):351–451.
- [5] Boulanger RW, Truman SP. Void redistribution in sand under post-earthquake loading. Can Geotech J 1996;33(5):829–34.
- [6] El Ghoraiby MA, Park H, Manzari MT. Stress-strain behavior and liquefaction strength characteristics of Ottawa F65 sand. Soil Dynam Earthq Eng 2020;138: 106292.
- [7] Arulanandan K, Scott R. Verification of numerical procedures for the analysis of soil liquefaction problems: proceedings of the international conference on the verification of numerical procedures for the analysis of soil liquefaction problems. Davis, California, USA. 1993. p. 17–20. October 1993. Rotterdam Brookfield: A.A. Balkema.
- [8] Brandenberg SJ, Boulanger RW, Kutter BL, Chang D. Behavior of pile foundations in laterally spreading ground during centrifuge tests. J Geotech Geoenviron Eng 2005;131(11):1378–91.
- [9] Kutter BL, Carey TJ, Hashimoto T, Zeghal M, Abdoun T, Kokkali P, Madabhushi G, Haigh SK, Burali d'Arezzo F, Madabhushi S, Hung W-Y, Lee C-J, Cheng H-C, Iai S, Tobita T, Ashino T, Ren J, Zhou Y-G, Chen Y-M, Manzari MT. LEAP-GWU-2015 experiment specifications, results, and comparisons. Soil Dynam Earthq Eng 2018; 113:616–28.

- [10] Cox BR. Development of a direct test method for dynamically assessing the liquefaction resistance of soils in situ. PhD Dissertation: The University of Texas at Austin; 2006.
- [11] Andrus RD, Youd TL. Subsurface investigation of a liquefaction-induced lateral spread, Thousand Springs Valley, Idaho. Department of Civil Engineering Brigham Young University; 1987. p. 131.
- [12] Towhata I, Maruyama S, Kasuda KI, Koseki J, Wakamatsu K, Kiku H, Kiyota T, Yasuda S, Taguchi Y, Aoyama S, Hayashida T. Liquefaction in the Kanto region during the 2011 off the pacific coast of Tohoku earthquake. Soils Found 2014;54 (4):859–73.
- [13] Ghafghazi M, DeJong JT. A review of liquefaction case histories in gravelly soils using SPT-based triggering curves. GeoVancouver 2016. Vancouver, BC, Canada: Canadian Geotechnical Society; 2016.
- [14] Dhakal R, Cubrinovski M, Bray J, de la Torre C. Liquefaction assessment of reclaimed land at Centreport, Wellington. Bull N Z Soc Earthq Eng 2020;53(1): 1–12.
- [15] Pires-Sturm AP, DeJong JT. Liquefaction potential and dynamic response of coarse-grained gravelly soils. J Geotech Geoenviron Eng 2021. Submitted 11/2020).
- [16] Sturm AP. On the liquefaction potential of gravelly soils: characterization, triggering and performance. Davis. PhD Dissertation: University of California; 2019.
- [17] Chapuis RP. Predicting the saturated hydraulic conductivity of sand and gravel using effective diameter and void ratio. Can Geotech J 2004;41(5):787–95.
- [18] Garnier J, Gaudin C, Springman SM, Culligan PJ, Goodings D, Konig D, Kutter BL, Phillips R, Randolph MF, Thorel L. Catalogue of scaling laws and similitude questions in geotechnical centrifuge modelling. Int J Phys Model Geotech 2007;7 (3):1–23.
- [19] Dobry R, Idriss IM, Ng E. Duration characteristics of horizontal components of strong-motion earthquake records. Bull Seismol Soc Am 1978;68(5):1487–520.
- [20] Muscolino G, Genovese F, Biondi G, Cascone E. Generation of fully non-stationary random processes consistent with target seismic accelerograms. Soil Dynam Earthq Eng 2021;141:106467.
- [21] Kamai R, Boulanger RW. Characterizing localization processes during liquefaction using inverse analyses of instrumentation arrays. Meso-Scale Shear Phys. Earthq. Landsl. Mech. 2011;219–38.
- [22] Carey TJ, Gavras A, Kutter BL, Haigh SK, Madabhushi SPG, Okamura M, Kim DS, Ueda K, Hung WY, Zhou YG, Liu K, Chen YM, Zeghal M, Abdoun T, Escoffier S, Manzari M. A new shared miniature cone penetrometer for centrifuge testing. In: Physical modelling in geotechnics. CRC Press; 2018. p. 293–8.
- [23] Sawyer BD. Cone penetration testing of coarse-grained soils in the centrifuge to examine the effects of soil gradation and centrifuge scaling. Master's Thesis. Davis: University of California; 2020.
- [24] Pires-Sturm AP, DeJong JT. Cone penetration resistance in coarse-grained gravelly soils. J Geotech Geoenviron Eng 2021. Submitted 11/2020).
- [25] Elgamal A, Yang Z, Lai T, Kutter BL, Wilson DW. Dynamic response of saturated dense sand in laminated centrifuge container. J Geotech Geoenviron Eng 2005;131 (5):598–609.
- [26] Kulasingam R, Malvick EJ, Boulanger RW, Kutter BL. Strength loss and localization at silt interlayers in slopes of liquefied sand. J Geotech Geoenviron Eng 2004;130 (11):1192–202.
- [27] Zamani A, Xiao P, Baumer T, Carey TJ, Sawyer B, DeJong JT, Boulanger RW. Mitigation of liquefaction triggering and foundation settlement by MICP treatment. J Geotech Geoenviron Eng 2021;147(10):040210.

- [28] Fiegel GL, Kutter BL. Liquefaction mechanism for layered soils. J. Geotechn. Eng. 1994;120(4):737–55.
- [29] Kokkali P, Abdoun T, Zeghal M. Physical modeling of soil liquefaction: overview of LEAP production test 1 at Rensselaer Polytechnic Institute. Soil Dynam Earthq Eng 2018;113:629–49.
- [30] Carey TJ, Stone N, Kutter BL, Hajialilue-Bonab M. A new procedure for tracking displacements of submerged sloping ground in centrifuge testing. In: Proceedings 9th international Conference on physical Modeling in geotechnics. London, UK: ICPMG 2018; 2018. p. 829–34.
- [31] Sinha SK, Kutter BL, Wilson DW, Carey TJ, Ziotopoulou K. Use of Photron cameras and TEMA software to measure 3D displacements in centrifuge tests. Davis, CA: Center for Geotechnical Modeling, Department of Civil and Environmental Engineering, University of California; 2021. p. 76. Report No. UCD/CGM-21/01.
- [32] White DJ, Take WA, Bolton MD. Soil deformation measurement using particle image velocimetry (PIV) and photogrammetry. Geotechnique 2003;53(7):619–31.
- [33] Stanier SA, Blaber J, Take WA, White DJ. Improved image-based deformation measurement for geotechnical applications. Can Geotech J 2016;53(5):727–39.
- [34] Randolph MF, Gaudin C, Gourvenec SM, White DJ, Boylan N, Cassidy MJ. Recent advances in offshore geotechnics for deep water oil and gas developments. Ocean Eng 2011;38(7):818–34.
- [35] Cilingir U, Madabhushi SPG. A model study on the effects of input motion on the seismic behaviour of tunnels. Soil Dynam Earthq Eng 2011;31(3):452–62.

- [36] DeJong JT, Randolph MF, White DJ. Interface load transfer degradation during cyclic loading: a microscale investigation. Soils Found 2003;43(4):81–93.
- [37] Kennedy R, Take WA, Siemens G. Geotechnical centrifuge modelling of retrogressive sensitive clay landslides. Can Geotech J 2021;58(10):1452–65.
- [38] Elshafie M, Choy C, Mair R. Centrifuge modeling of deep excavations and their interaction with adjacent buildings. Geotech Test J 2013;36(5).
- [39] Ritter S, Giardina G, DeJong MJ, Mair RJ. Centrifuge modelling of building response to tunnel excavation. Int J Phys Model Geotech 2018;18(3):146–61.
- [40] Carey TJ, Chiaradonna A, Love N, DeJong JT, Ziotopoulou K, Martinez A. Effect of soil gradation on the response of a submerged slope when subjected to shaking – centrifuge data report for TJC01. Center for Geotechnical Modeling, University of California Davis; 2021. Report No. UCD/CGM – 21/01.
- [41] Carey TJ, Love N, DeJong JT, Ziotopoulou K, Martinez A. Effect of soil gradation on the response of a submerged slope when subjected to shaking – centrifuge data report for TJC02. Center for Geotechnical Modeling, University of California Davis; 2021. Report No. UCD/CGM – 22/02.
- [42] Idriss IM, Boulanger RW. Soil liquefaction during earthquakes. Oakland: EERI MNO-12; 2008.
- [43] Kutter BL, Wilson DW. In: De-liquefaction shock waves. 7th US-Japan Workshop on earthquake resistant Design of lifeline Facilities and countermeasures against soil liquefaction, MCEER. 99; 1999. p. 295–310.